RESEARCH PAPER

Single-particle crushing behaviour of carbonate sands studied by X-ray microtomography and a combined finite–discrete element method

Bo Zhou[1] · Quan Ku[2] · Changheng Li[1] · Huabin Wang[1] · Youkou Dong[3] · Zhuang Cheng[4]

Abstract

This paper investigates the particle breakage behaviour of a carbonate sand based on single-particle compression experiments with in situ X-ray microtomography scanning (μCT) and a combined finite–discrete element method (FDEM). Specifically, X-ray μCT is applied to extract the information on grain morphology and intra-particle pores of carbonate sand particles to establish an FDEM model. The model is first calibrated by comparing the simulation results of two carbonate sand grains with the corresponding single-particle compression experiment results and then applied to model the stress evolution, cracking propagation and failure of other carbonate sand particles under single-particle compression. To study the influence of intra-particle pores, FDEM modelling of carbonate sands with completely filled intra-particle pores is also performed. The particle strength of carbonate sands both with and without pore filling is found to follow a Weibull distribution, with that of the sand with pore filling being considerably higher. This behaviour is associated with lower stress concentration, resulting in later crack development in the pore-filled sand than in the sand without pore filling. The cracks are found to usually pass through the intra-particle pores. Consequently, a larger proportion of particles fail in the fragmentation mode in the sand without pore filling.

1 Introduction

Carbonate sands are a highly crushable type of sand, mainly composed of the skeletal remains of marine organisms such as corals, shells, coccoliths and foraminifera. They are widespread in the warm and shallow seas of tropical and subtropical regions and have been used as backfill materials in many engineering structures such as foundations, embankments and airport runways. Carbonate sands have highly irregular grain shapes and abundant cavities and intra-particle pores, as shown in Fig. 1. Their engineering properties differ considerably from those of quartz sands. Carbonate sands usually exhibit a higher peak stress ratio than quartz sands at low stress levels and more grain breakage at high stress levels because of their greater interlocking effects caused by the more irregular grain morphologies [6, 14, 15]. The higher susceptibility to grain breakage under high stress can be attributed to the looser fabric of carbonate sands, resulting from the abundant intra-particle pores and the lower grain strength relative to quartz sands [24, 26]. Hence, compared with quartz sands, carbonate sands can more easily cause problems (e.g. low load-bearing capacity of driving piles and large displacements of embankments and airport runways) when used in engineering applications [1, 13, 22, 31, 41]. Therefore, fundamental research on the mechanical behaviour of carbonate sands, particularly the effects of their grain

✉ Zhuang Cheng
  zhuangcheng@whut.edu.cn

1 School of Civil and Hydraulic Engineering, Huazhong University of Science and Technology, Wuhan, China

2 Department of Civil and Environmental Engineering, The Hong Kong University of Science and Technology, Hong Kong, China

3 College of Marine Science and Technology, China University of Geosciences, Wuhan, China

4 School of Civil Engineering and Architecture, Wuhan University of Technology, Wuhan, China
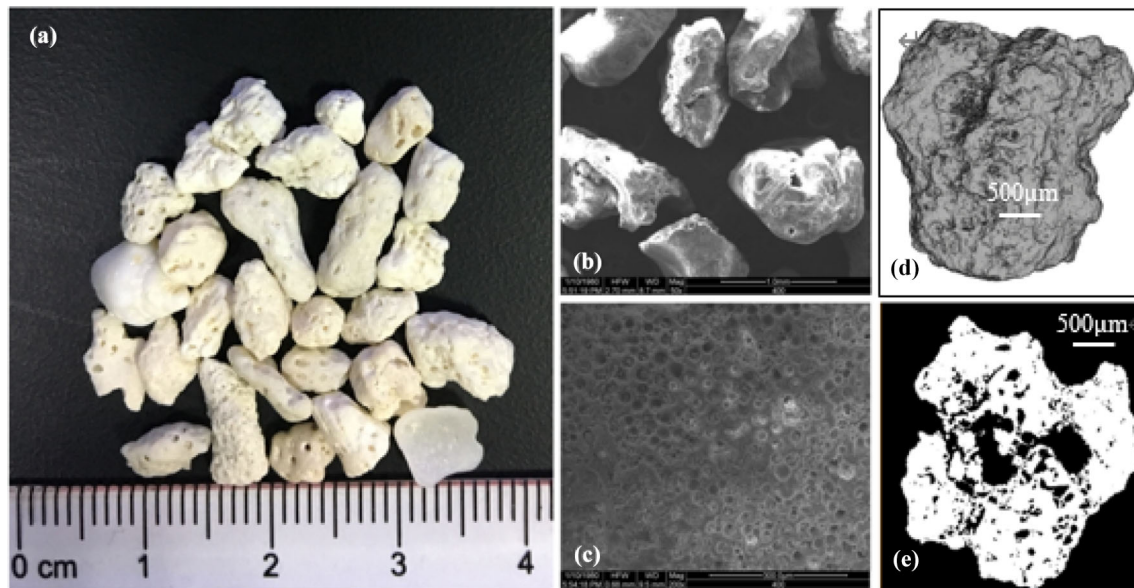
Fig. 1 Images of typical carbonate particles: **a** photograph; **b** scanning electron microscopy (SEM) image at 50 × magnification; **c** SEM image at 400 × magnification; **d** volumetric rendering and **e** a cross section of a carbonate particle

morphologies and intra-particle pores, is urgently needed to facilitate their safe use in engineering applications.

Particle morphology plays an important role in the mechanical behaviour of sands. To quantify particle morphological features, particle shape parameters, such as grain sphericity, roundness, convexity and fractal dimensions, have been defined [20, 32, 52], and several methods based on projected 2D or 3D images of sand particles have been developed to quantify these parameters [3, 5, 34, 35, 42, 48, 50, 51]. In particular, X-ray microtomography (μCT) has become a powerful tool for the acquisition of 3D particle CT images with a high spatial resolution on the order of microns. μCT has been increasingly used for the quantification of grain size and grain morphology [24, 46, 47, 52] and the non-destructive measurement of micromechanical behaviour of soils, such as grain kinematics, inter-particle contact fabric and strain localisations [4, 9, 10, 12, 17, 37]. Using X-ray μCT, several scholars have investigated the evolution of particle size and particle morphology of carbonate sands under different loading conditions [11, 24, 33].

The high precision of X-ray μCT in particle shape quantification has facilitated the numerical modelling of realistic particle shapes based on CT images. For instance, methods such as the micro-finite element method, level-set discrete element method, spherical harmonic discrete element method and combined finite element method/discrete element method (FDEM) have been applied to model the micromechanical behaviour of sand under triaxial compression based on the CT images acquired from in situ triaxial testing with CT scanning [8, 23, 28, 38].

Furthermore, DEM and FDEM have been adopted to model the mechanical behaviour of sand particles under different loading conditions with realistic consideration of the sand grain shapes [19, 39, 43, 53]. These studies have highlighted the important role of grain morphology in the mechanical behaviour of sands. However, in most of these numerical studies, the modelled quartz sands contained few or no intra-particle pores, thus ruling out any insights into the effects of such pores on the sand mechanical behaviour. For carbonate sands, which feature both highly irregular grain shapes and abundant intra-particle pores, it is necessary to consider both of these features to achieve more realistic modelling.

This paper presents the FDEM modelling of carbonate sand particles under single-particle compression, incorporating quantitative information on both realistic grain morphologies and intra-particle pores obtained by X-ray μCT. The remainder of this paper is organised into four sections. Section 2 presents the methodology of CT image-based FDEM modelling. Specifically, Sect. 2.1 introduces the tested carbonate sand and the apparatus for the single-particle compression experiments with in situ X-ray μCT scanning. The experiments are performed to acquire the grain geometrical data and particle crushing behaviour of the sand grains for FDEM model establishment and calibration. Section 2.2 presents the image processing and analysis techniques for extracting information on the grain morphology and intra-particle pores of the sand grains from their CT images. Section 2.3 briefly introduces the combined FDEM modelling method. Sections 3–4 elaborate on the calibration of the FDEM model and the

implementation of the model to study the crushing behaviour of the sand grains and the influence of intra-particle pores. Section 5 presents the conclusions of this study.

2 Methodology

2.1 Test materials and miniature loading apparatus

The test materials were coarse carbonate particles sampled from the Spratly Islands, South China Sea [49]. The particles had a diameter of 3.0–5.0 mm and high proportions of intra-particle voids (0.025–0.275), namely enclosed voids inside the particle body. A typical carbonate particle with intra-particle porosity of 0.142 is presented in Fig. 1d and e. Due to the biological origin of carbonate sand, various patterns could be observed on the particles, such as elongated corals, bladed shells and blocky clasts of ancient reef limestone. Figure 2 depicts typical carbonate particles with these three patterns. Generally, for intact particles without internal voids, blocky particles have higher particle strength than the elongate particles and platy particles [2]. In this study, 38 carbonate particles including these three patterns were randomly selected for the single-particle crushing experiments. Among them, two grains were used for single-particle crushing experiments with in situ X-ray μCT scanning. The others were placed into a cylindrical container by air pluviation. They were scanned using the same X-ray μCT system to acquire their morphological and intra-particle pore data for image-based FDEM modelling.

To perform single-particle crushing experiments with in situ X-ray μCT scanning, a miniature uniaxial compression loading apparatus was specially fabricated. Figure 3a–c depicts schematics of the loading apparatus and its combined use with an X-ray μCT scanner. The apparatus has a structure similar to that used in [46]. It consists of four major parts: a sample chamber, a loading system, a data acquisition and controlling system, and a loading frame. As seen in Fig. 3a, the sample chamber is located at the top of the apparatus, which is made of lightweight, high-strength and radiolucent poly(ether-ether-ketone) (PEEK). The chamber is used as a container which enables the functioning of X-ray μCT scanning of the single grain within it. To load a particle, the screw rod driven by a stepping motor slowly moves towards the top steel cap inside the tube. The stepping motor can supply a maximum load of 1.0 kN and a minimum loading speed of 0.01 mm/min. In another word, a minimum strain rate of 0.25%/min for a particle with a diameter of 4 mm can be reached. The measuring range and precision are 500 N and 0.1% for the load cell, and 20 mm and 0.02% for the displacement sensor, respectively. The settings were chosen to ensure that the loading apparatus provided reliable load–displacement data in the single-particle crushing experiment.

During the experiment, the loading apparatus was fixed onto the rotation base within an X-ray μCT system (Phoenix v|tome|x m, GE, Shanghai, China), which contains an X-ray tube, a rotation base and a detector, as shown in Fig. 3b and c. To carry out the experiment, a carbonate particle was first coated with silicon grease and placed between the two PEEK loading plates. The silicone grease can effectively prevent the fragments exploding out of the scanning region once the particle breakage occurs. It was then axially compressed at a constant rate of 0.1 mm/min. The loading was paused twice at two loading states to perform CT scanning. The first scan was taken at a loading force of approximately 10 N to image the original particle morphology and intra-particle voids of the tested particle. This loading is sufficient to fix the particle during scanning but does not lead to crack initiation. The second scan was taken after major fractures emerged within the particle to acquire an image of the generated cracks and fragments. During each scan, the axial displacement remained unchanged while the rotation base rotated the apparatus through 360 degrees to acquire the particle CT images (Fig. 3c). For each scan of the particle, a stack of CT slices (i.e. 2795 slices) of dimension 2036 × 2036 pixels and spatial resolution 6.6 μm/pixel was acquired.
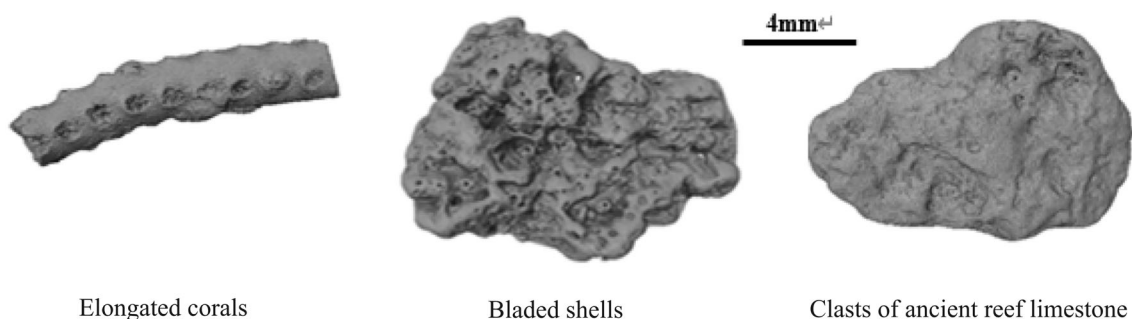

Fig. 2 Typical carbonate particles with different patterns

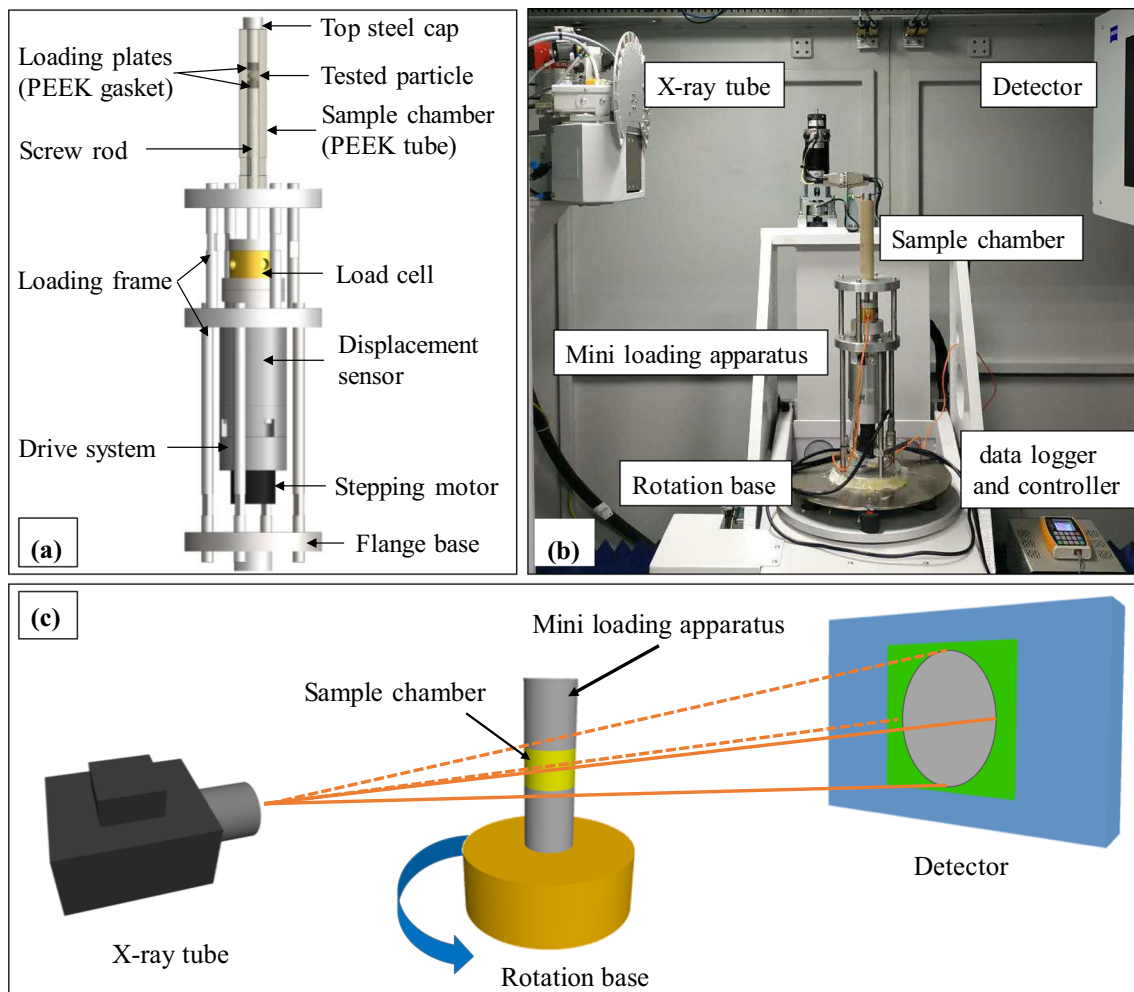| Elongated corals | Bladed shells | Clasts of ancient reef limestone |

4mm

Fig. 3 Schematic of the experimental setup: **a** structural components of the loading apparatus; **b** loading apparatus within a μCT system; **c** sample during X-ray μCT scanning

2.2 Image acquisition and processing

To quantify the generated cracks and fragments of the tested particle, it is necessary to extract individual fragments from the raw 3D particle CT images by implementing a series of image processing steps. Typically, image processing includes noise reduction, phase segmentation and region separation, which was implemented using MATLAB. Figure 4a–i presents the image processing results for a CT slice of a fractured carbonate particle. Note that 3D CT images were processed in this study. First, a median filter of size $3 \times 3 \times 3$ pixels was applied twice to the raw CT image (Fig. 4a) to remove image noise, as seen in the close-up views in Fig. 4b and c. Then, image binarisation was applied to the filtered CT image to identify the carbonate fragment phase based on an automatic thresholding technique [30]. The result was a binary image like that shown in Fig. 4d, in which the sand phase is in white and the void phase and the crack phase are in black.

As the binary image contains numerous intra-particle voids and surface concaves, a direct application of watershed segmentation to the image generally results in severe over-segmentation. Therefore, these intra-particle voids and surface concaves were filled prior to the watershed segmentation. This step was achieved by successively implementing the morphological operations of hole filling, image closing and hole filling on the binary image. A disc-shaped structural element of radius five pixels, determined based on a parameter study, was used for image closing. The newly generated grain phase voxels during the morphological operations were recorded. The resulting images acquired during hole filling, image closing and hole filling are shown in Figs. 4e, f and g, respectively. Next, a watershed algorithm [40] was applied to the image to separate the individual fragments, which were stored in a labelled image, as shown in Fig. 4h. Lastly, the additional grain phase voxels that emerged during the morphological operations were removed from the segmented CT image
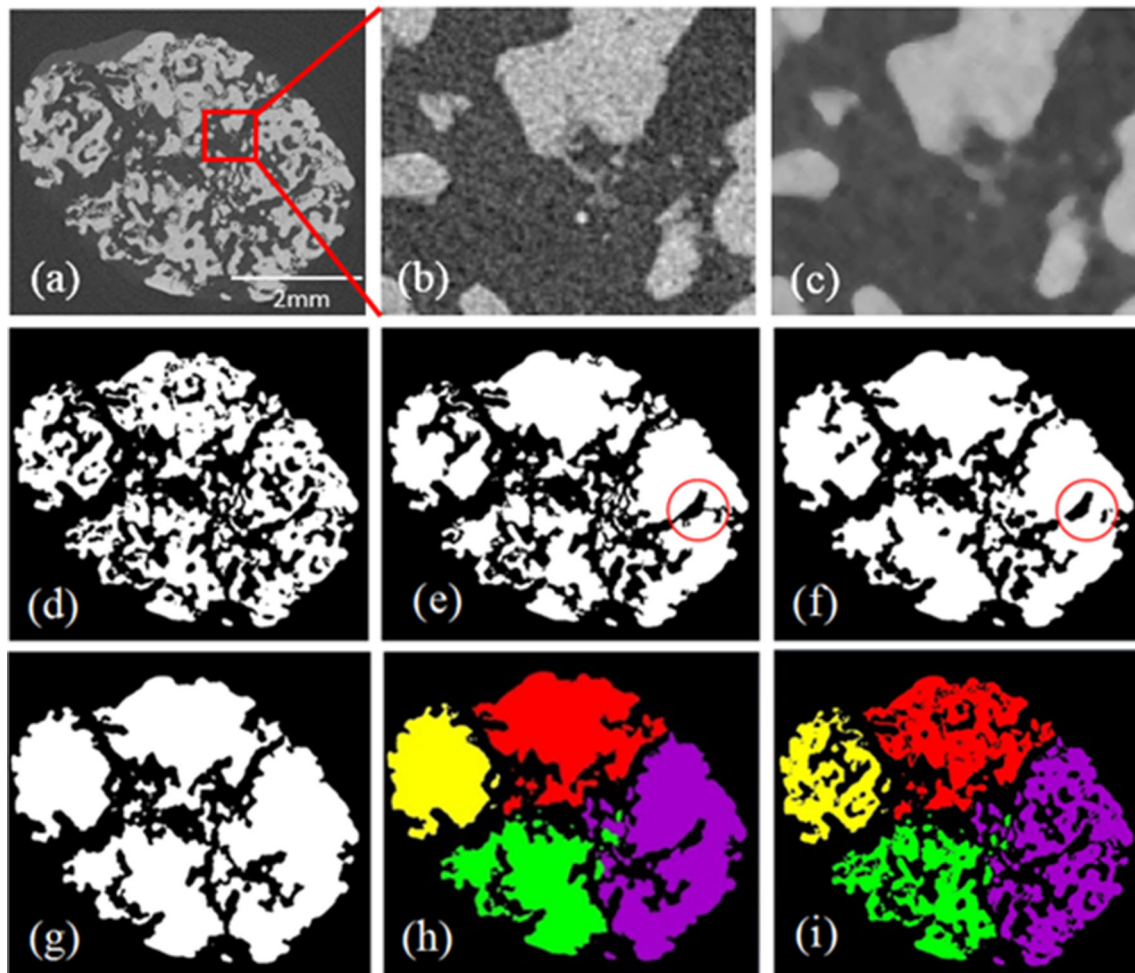
Fig. 4 Image processing procedure for fragment segmentation from the µCT images of a fractured carbonate particle: **a** a raw CT slice; **b** a close-up view of **a**); **c** after median filtering of **b**); **d** after image binarisation; **e** after the first hole filling operation; **f** after image closing; **g** after the second hole filling operation; **h** labelled image after watershed segmentation; and **i** labelled image after rebuilding the intra-particle pores and surface concaves

(Fig. 4h) to rebuild the intra-particle voids and surface concaves of the carbonate fragments. The final resulting image of the separated sand fragments is shown in Fig. 4i, in which different fragments are marked with different colours. Figure 5 shows a volume rendering of the CT images of the labelled fragments of the tested carbonate particles before and after image processing.

The same image processing techniques were applied to the CT images of the cylindrical sample to identify and extract the individual grains. Figure 6 presents a 3D volumetric rendering of µCT images the extracted individual grains, which forms a database of particle morphology and intra-particle voids for the FDEM modelling.

2.3 Combined FDEM modelling

In this study, a combined FDEM method [53] was used to model the single-particle crushing behaviour of carbonate sands with realistic grain shapes and intra-particle voids. The combined FDEM method combines a finite element modelling (FEM) scheme and a discrete element modelling (DEM) scheme to execute the calculations. Specifically, the FEM scheme is adopted to calculate the stress and strain fields of solid elements and evaluate whether fractures occur. Meanwhile, the FEM scheme is also utilized to detect contacts of discrete elements and calculate the contact forces based on the elements' deformation. Whereas the DEM scheme is used to calculate the motion of discrete elements based on Newton's Second law. In particular, tetrahedral finite elements with flexible sizes and shapes can be applied via the FEM scheme to reconstruct the complex particle morphology and intra-particle voids of granular materials. Therefore, FDEM is particularly suitable for simulating particle stress fields and particle breakage behaviour of carbonate particles. In this study, the FDEM simulation was conducted using the
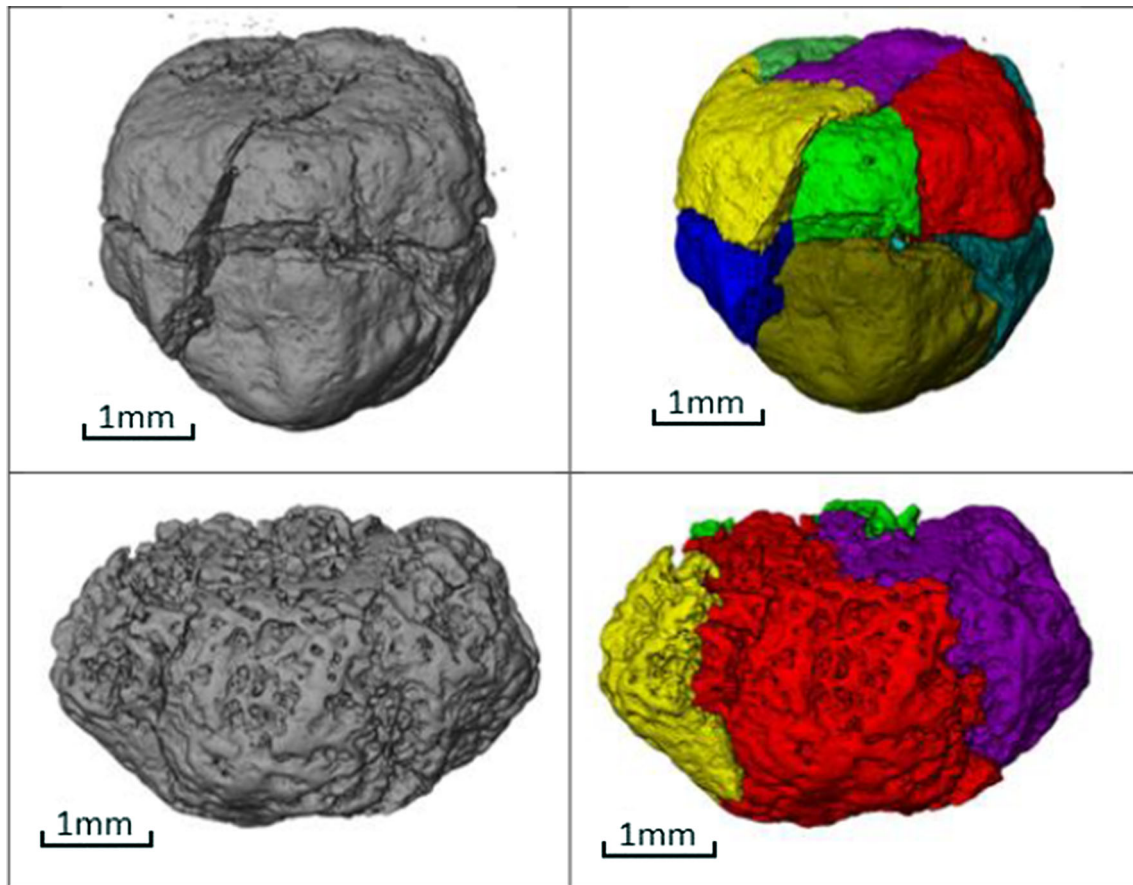
Fig. 5 Volume rendering of μCT images of the fractured fragments of two carbonate particles before and after image processing
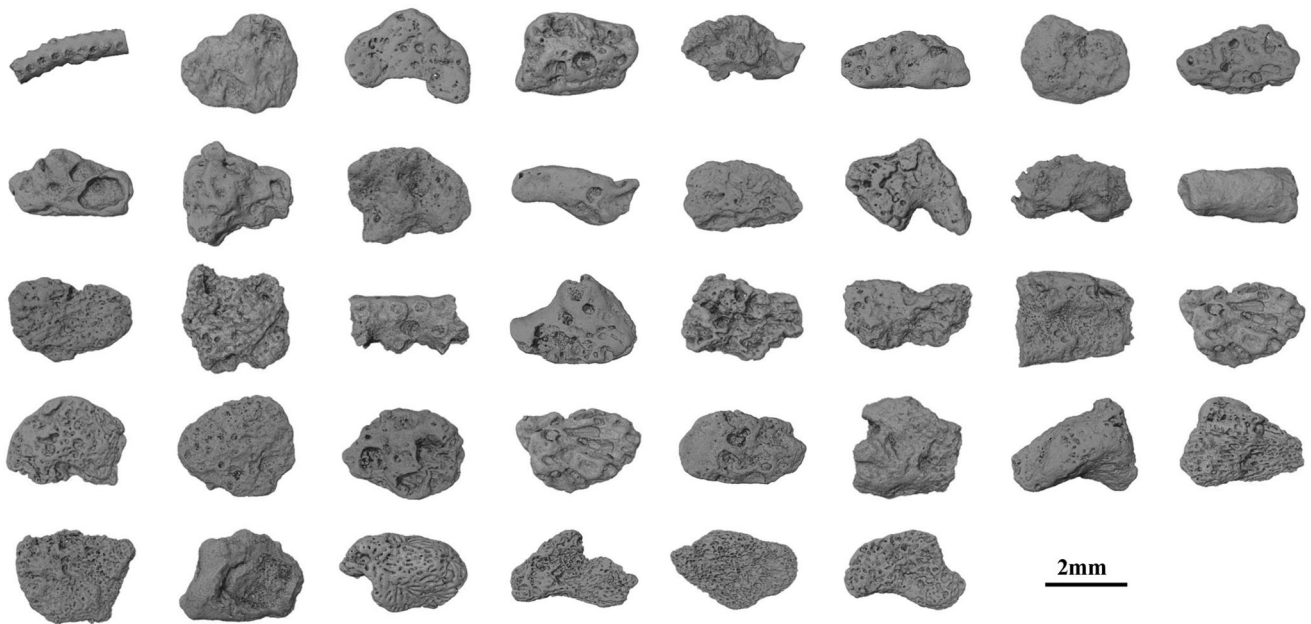

Fig. 6 3D Volume rendering of μCT images of individual carbonate grains

Abaqus/Explicit platform, which has been shown to have a high computation capacity for simulating physical problems involving a large number of contacts between discrete elements [16].

Figure 7a-d presents the process to establish the FDEM model of a carbonate particle based on its CT image. First, an open-source 3D mesh generation toolbox, *iso2mesh*, based on the MATLAB platform [18] was applied to the CT image to generate a refined Delaunay triangulation mesh of the external and internal particle surfaces (Fig. 7b). Then, the surface mesh was imported into Abaqus to generate solid tetrahedral elements of the particle volume (Fig. 7c). To balance the model precision and computational efficiency, the mesh size of the tetrahedral elements was set to approximately 0.1 mm, leading to approximately 10,000 tetrahedral elements for the carbonate particle. To model solid fractures, triangular cohesive interface elements (CIEs) with geometric zero-thickness were embedded between the faces of each pair of adjacent tetrahedral elements, as seen in Fig. 7c. Fractures were allowed to occur along the faces if the corresponding CIEs failed according to a traction–separation damage law [21, 44]. Finally, a pair of loading platens was added to the model, as seen in Fig. 7d.

In the FDEM simulation, a linear elastic constitutive model was used to simulate the mechanical behaviour of the tetrahedral elements. With regard to CIEs, a bilinear function was used to define the relationship between their deformation and failure states, as suggested in previous studies [53].

Specifically, the relationship between the interface traction $\boldsymbol{\sigma} = (\sigma_\mathrm{n}, \sigma_\mathrm{s}, \sigma_\mathrm{t})$ and the relative displacement $\boldsymbol{\delta} = (\delta_\mathrm{n}, \delta_\mathrm{s}, \delta_\mathrm{t})$ of a CIE is defined by

$$\boldsymbol{\sigma} = \mathbf{K}\boldsymbol{\delta}, \tag{1}$$

$$\mathbf{K} = \begin{bmatrix} k_\mathrm{nn} & 0 & 0 \\ 0 & k_\mathrm{ss} & 0 \\ 0 & 0 & k_\mathrm{tt} \end{bmatrix} \tag{2}$$

where $\mathbf{K}$ is the stiffness matrix of the CIE, and n, s and t denote the normal and two shear directions, respectively.

In the FDEM model, a crack initiates if the maximum nominal stress $\sigma_\mathrm{norm}^{max}$ defined by Eq. (3) has a value of 1.

$$\sigma_\mathrm{norm}^{max} = \max\left\{\frac{\sigma_\mathrm{n}}{\sigma_\mathrm{n}^0}, \frac{\sigma_\mathrm{s}}{\sigma_\mathrm{s}^0}, \frac{\sigma_\mathrm{t}}{\sigma_\mathrm{t}^0}\right\}, \tag{3}$$

$$\sigma_n = \begin{cases} \sigma_n, & for\ \sigma_n > 0 \\ 0 & for\ \sigma_n \le 0 \end{cases}.$$

Here, σ_n^0, σ_s^0 and σ_t^0 are model parameters representing the ultimate tensile and tangential stresses of the CIE, respectively.

The stiffness matrix $\mathbf{K}$ is assumed to be constant for each CIE prior to crack initiation. The magnitudes of its elements decrease during the crack opening until reaching 0, indicating the failure of CIE. The elements of $\mathbf{K}$, k_mm ($m = n$, s or t), can be determined as
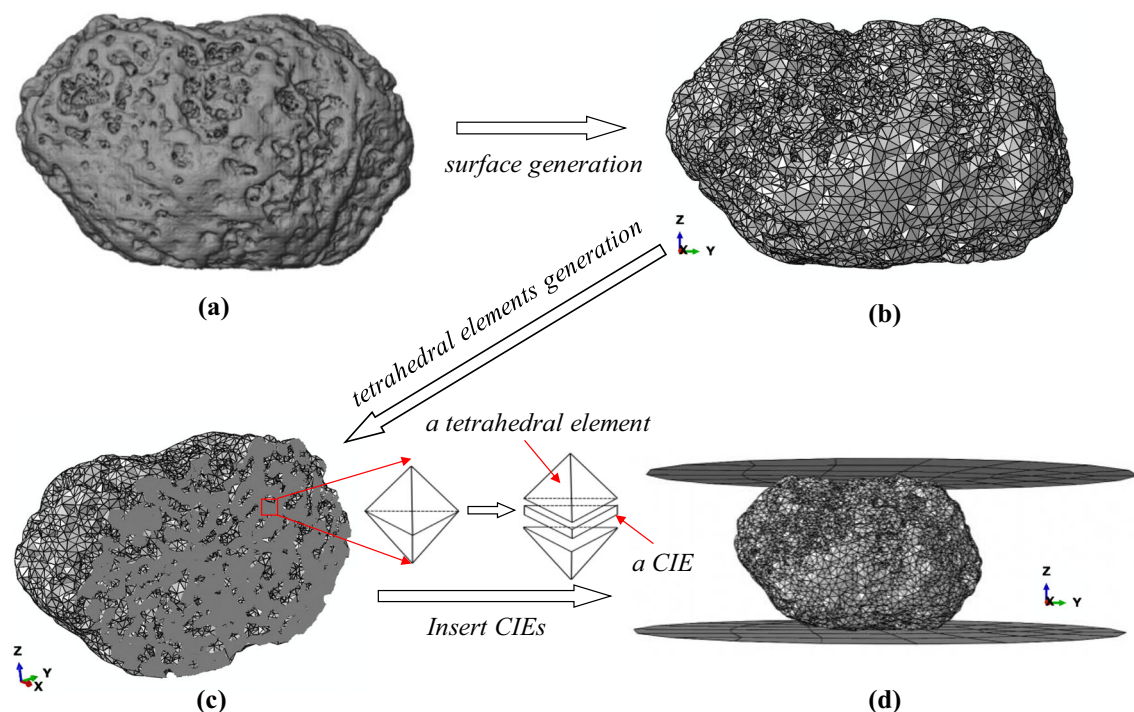

Fig. 7 FDEM modelling of single-particle crushing experiments: **a** CT image of a carbonate particle; **b** Delaunay triangulation mesh of the particle surfaces; **c** particle solid tetrahedral elements with CIEs; **d** particle FDEM model with loading platens

$$k_{mm} = k_m^0, \text{ prior to crack initiation} \quad (4)$$

$$k_{mm} = (1 - D)k_m^0, \text{after crack initiation} \quad (5)$$

$$D = \frac{\delta_m^f(\delta_m^{max} - \delta_m^0)}{\delta_m^{max}(\delta_m^f - \delta_m^0)}, \quad (6)$$

Here, k_m^0 ($m = n$, s or t) and D are the Young's modulus and a damage variable of the CIE, respectively. δ_m^{max} ($m = n$, s or t) is the maximum displacement of the CIE during its loading history. δ_m^0 ($m = n$, s or t) and δ_m^f ($m = n$, s or t) are the corresponding displacements at the moments of crack initiation and ultimate failure of CIE, respectively.

Note that δ_m^f in Eq. (6) is related to the fracture energy release rate G_f as follows:

$$\delta_m^f = \frac{2G_f}{\sigma_{eff}^0} \quad (7)$$

Here, $\sigma_{eff}^0 = \sqrt{\sigma_n^2 + \sigma_s^2 + \sigma_t^2}$ is the relative effective traction stress at crack initiation.

According to the Benzeggagh–Kenane criterion [27], G_f can be determined based on the corresponding fracture energy release rates for pure mode I (tension) G_n and pure mode II (shearing) G_s and G_t. In this study, an isotropic failure mode of CIEs for which $G_f = G_n$ was assumed for simplicity.

3 Calibration of the FDEM model

In simulating the carbonate particle under uniaxial compression, the bottom loading platen (Fig. 7d) was fixed and the upper loading platen was moved vertically downwards with a constant velocity of 0.01 m/s. The friction coefficient between the loading platens and the sand particle was set to 0.5 to restrain the translation and rotation of the particle during the loading. The other FDEM model parameters were carefully calibrated by comparing the numerical results of two uniaxially compressed carbonate particles with the corresponding experimental results using a trial-and-error method. Specifically, empirical model parameters were first determined according to the material properties of carbonate minerals. Then, the Young's modulus and Poisson's ratio of the solid elements were slightly modified to ensure that the initial slopes of the load–displacement curves of the FDEM model results were consistent with the experimental results to the maximum extent. The physical parameters of CIEs for the FDEM model were initially selected based on a previous parametric study by the authors [53]. Adjustments of these parameters were made to optimise the agreement in the crushing force between the FDEM results and the

experimental results. The calibrated FDEM model parameters for the carbonate sands are summarised in Table 1.

Figure 8a and b shows the load–displacement curves and the 3D views before and after failure of the two tested carbonate particles from the FDEM simulations, respectively. For ease of visualisation, the corresponding experimental results are also plotted. Figure 9 presents the fracture patterns of the tested particles on a vertical section based on the experiments and FDEM simulations. As seen from Figs. 8 and 9, both the load–displacement curves and the fracture patterns from the FDEM simulations agree well with the corresponding experimental results. For both carbonate particles, the difference in peak loading force between the simulation and the experiment is within 20%, as seen in Fig. 8. We can see from Fig. 9 that the multiple fragments produced from the FDEM models have similar grain shapes to those from the experiments for both carbonate particles. These phenomena indicate that the FDEM model is highly effective for simulating the fracture behaviour of carbonate particles using the current model parameters.

4 Results and discussion

To explore the single-particle crushing behaviour, the calibrated FDEM model was applied to simulate the 38 carbonate particles under single-particle compression based on the CT images (Fig. 6). Parallel FDEM simulations of single-particle compression experiments on carbonate particles were also performed using the CT images of individual carbonate particles after all their intra-particle

Table 1 Physical and mechanical parameters used in FDEM simulations

| Parameter		Value
Bulk element	Density (kg/m³)	2700
	Elastic modulus (N/m²)	5×10^{13}
	Poisson's ratio	0.3
Cohesive element	Normal stiffness (N/m³)	5×10^{13}
	Tangential stiffness (N/m³)	3×10^{13}
	Tensile strength (N/m²)	2×10^5
	Shear strength (N/m²)	3×10^5
	Normal fracture energy (N/m)	100
	Tangential fracture energies (N/m)	100
Loading platen	Friction coefficient	0.5
	Stiffness	Infinity
System	Friction coefficient	0.5
	Damping coefficient	0.7
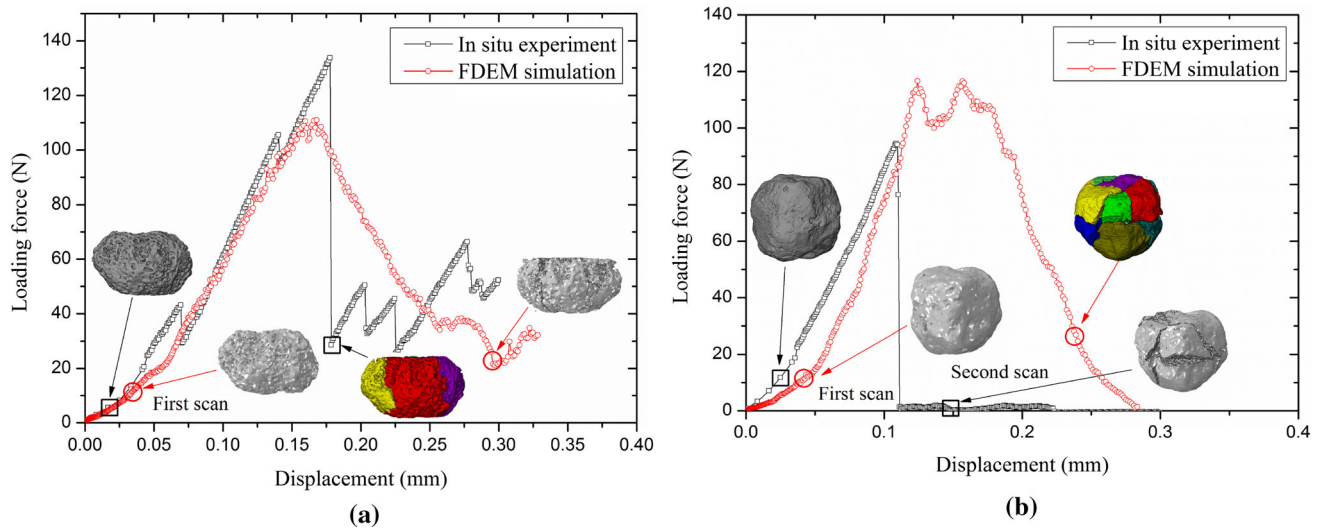
Fig. 8 Load–displacement curves of two carbonate particles and their 3D views before and after failure based on the experiments and FDEM simulations: **a** particle 1 and **b** particle 2
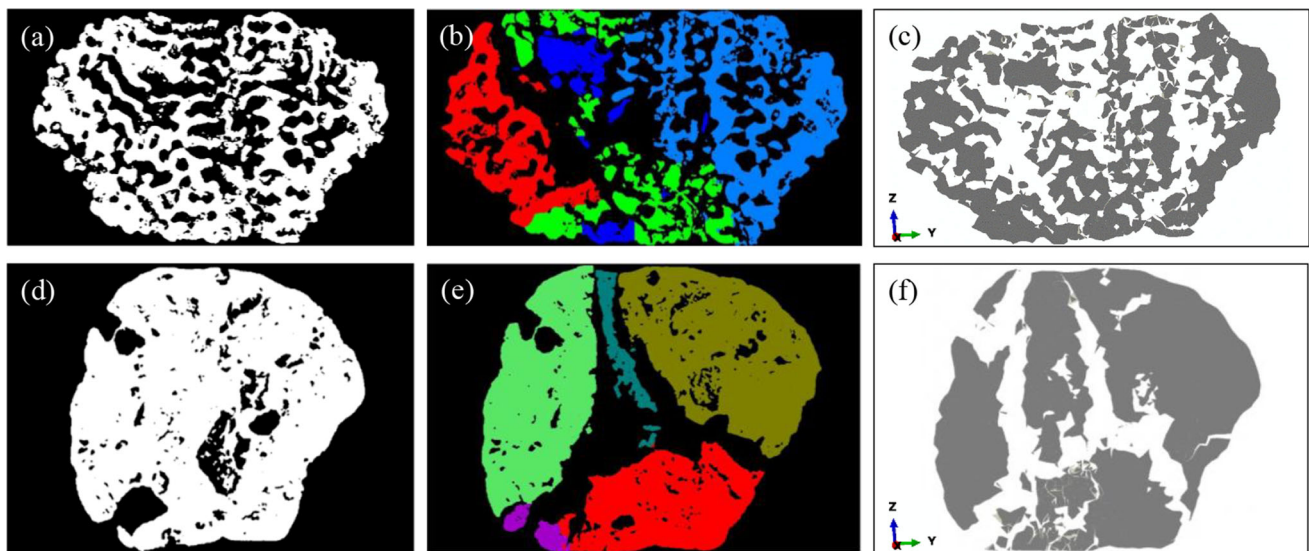

Fig. 9 Fracture patterns of the carbonate particles from experiments and FDEM simulations: **a** and **d** vertical sections of the intact particles; **b** and **e** vertical sections of the fractured particles based on the experiments, in which different colours represent different fragments; **c** and **f** vertical sections of the fractured particles based on FDEM simulations

pores were filled. This allows comparisons between the two groups of FDEM simulations to study the influence of intra-particle pores on the single-particle crushing behaviour. To implement the FDEM modelling, individual particles were usually rested on their major principal dimensions according to the minimal potential energy to avoid unstable particle rotation during the loading [19, 2, 25].

4.1 Particle crushing strength

For a single particle undergoing axial compression, the particle crushing strength can be represented by the maximum tensile stress σ_f within the particle volume [7, 36], as expressed by

$$\sigma_{\mathrm{f}} = \frac{0.9F}{d_2 d_3},\tag{8}$$

where F is the major peak force on the force–displacement curve, as shown in Fig. 7; d_2 and d_3 are the intermediate

and minor principal dimensions of the particle, respectively.

According to previous studies [29], the particle strength of a sand usually follows a Weibull distribution described by

$$P_s = \exp\left[-\left(\frac{\sigma_f}{\sigma_0}\right)^m\right] \tag{9}$$

where P_s is the survival probability of a sand particle under the maximum tensile stress σ_f; σ_0 is the characteristic tensile strength of the particle, which equals the maximum tensile stress when $P_s = 0.37$; m is the Weibull modulus, which reflects the degree of variability in the particle strength: higher m values indicate lower particle strength variability.

Clearly, Eq. (9) can be expressed in the following form:

$$\ln\left(\ln\left(\frac{1}{P_s}\right)\right) = m \ln \frac{\sigma_f}{\sigma_0}. \tag{10}$$

Figure 10a plots the variation of survival probability of sand grains with the maximum particle tensile stress for the carbonate sands with and without pore filling. The carbonate sands with pore filling have a distinctively higher survival probability than those without pore filling under any maximum particle tensile stress. The carbonate sands with and without pore filling have a σ_0 of 13.45 and 11.37 MPa, respectively. This indicates that intra-particle pores reduce the particle strength. This was found to be related to the different stress distributions within the sand grains, as discussed in Sect. 4.2. Figure 10b depicts the Weibull strength distribution curves for the carbonate sands with and without pore filling. There is a linear relationship between $ln\left(ln\left(\frac{1}{P_s}\right)\right)$ and $ln\left(\frac{\sigma_f}{\sigma_0}\right)$ for both

carbonate sands. Interestingly, the fitted lines for the two carbonate sands have very similar slopes (i.e. m values), indicating that the particle strength follows a Weibull distribution and that the two carbonate sands have the same degree of particle strength variability.

To discuss the influence of intra-particle porosity on the particle strength increase after pore filling, the particle strength increase rate vs. filled intra-particle porosity plot is presented in Fig. 11. Here, the particle strength increase rate is defined as the increase in particle crushing strength after pore filling divided by the particle crushing strength of the original particle (i.e. without pore filling). A moderate positive correlation is found between the particle strength increase rate and the intra-particle porosity, with a coefficient of determination of 0.44. The relatively low correlation coefficient might be attributable to the highly
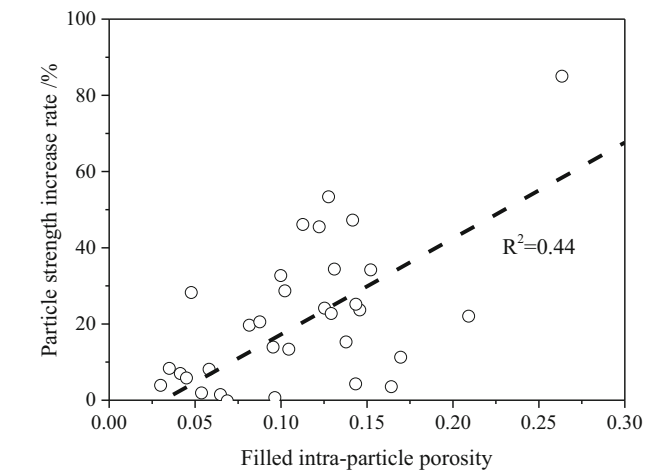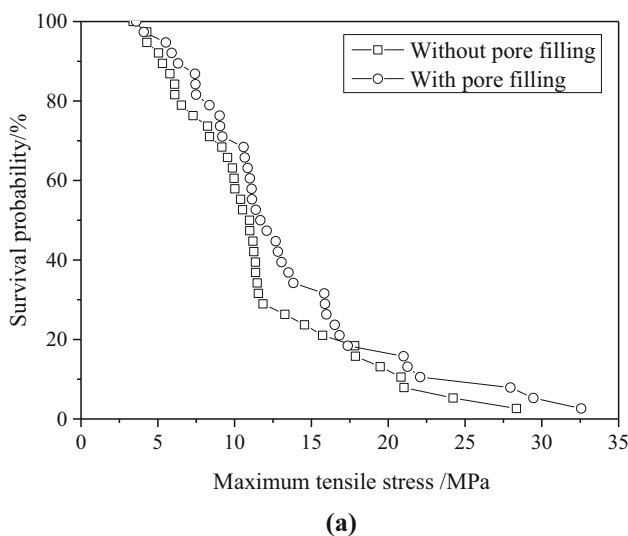
Fig. 11 Variation of particle crushing strength increase rate with intra-particle porosity
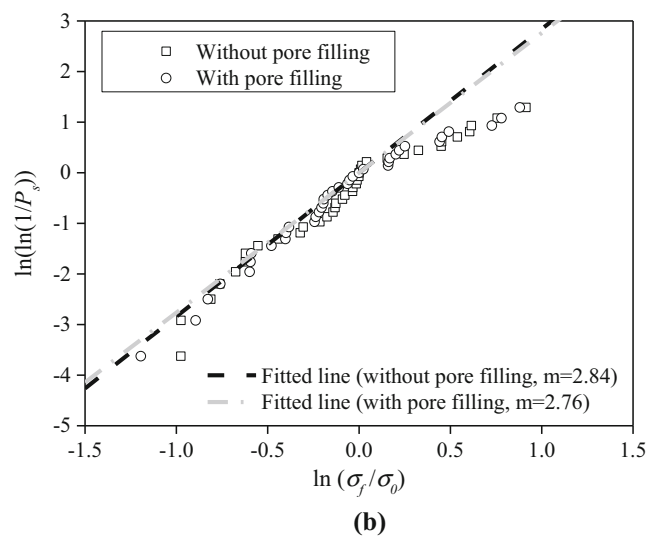
Fig. 10 a Particle survival probability of carbonate sands with and without pore filling; **b** Weibull strength distribution curves
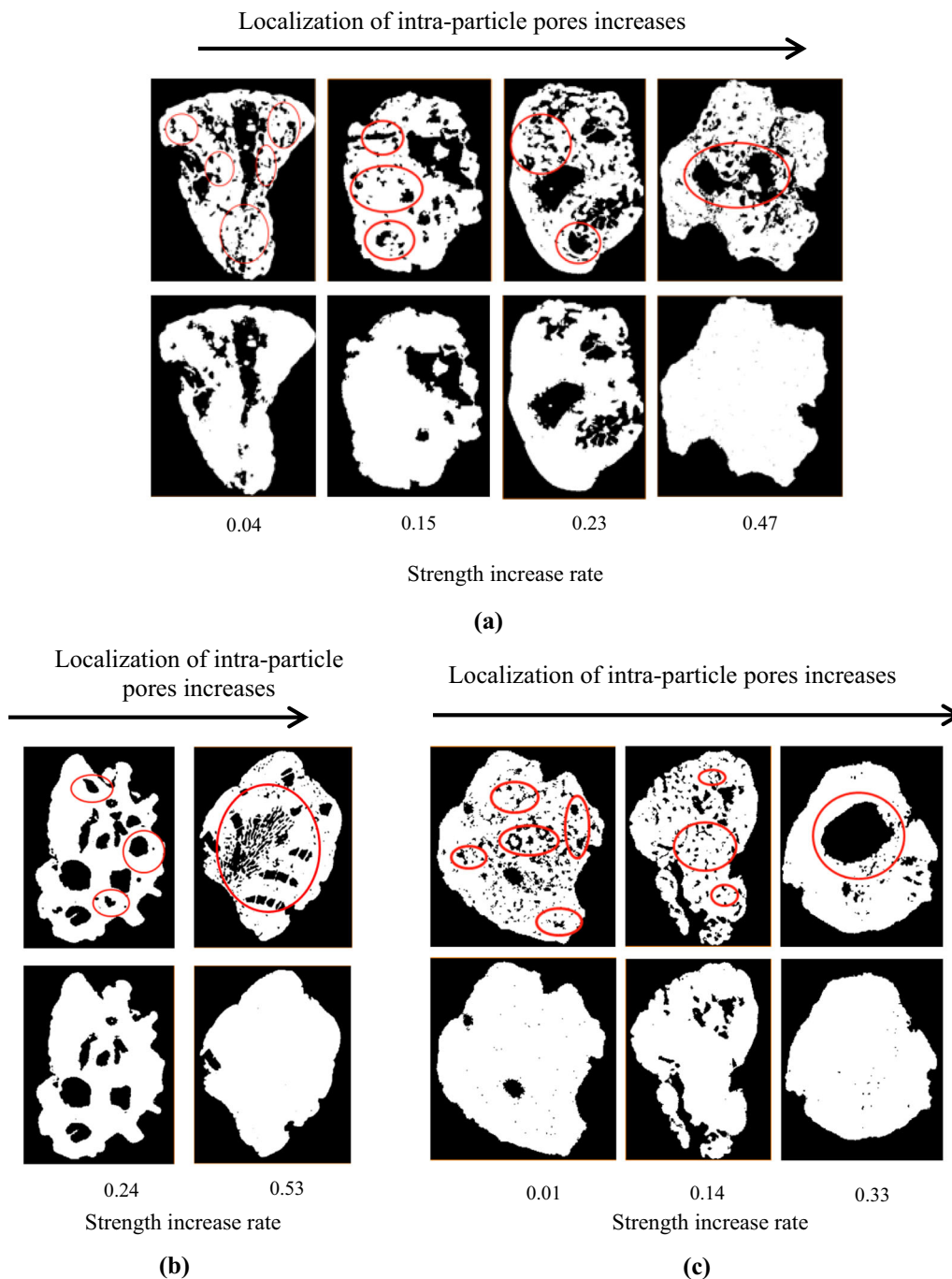
Fig. 12 Effects of intra-pore distribution on the strength increase rate of particles after pore filling: strength increase rate of particles with intra-particle porosity of around **a** 0.15; **b** 0.12 and **c** 0.09

heterogenous distribution of intra-particle pores and the highly irregular grain shapes of individual carbonate particles. However, the results fully reflect the fact that the particle strength can be significantly improved by filling the intra-particle pores, especially for the particles with high intra-particle porosities.

Apart from the intra-particle porosities, the pore distribution also has considerable influence on the strength increase rate. Figure 12a-c presents the strength increase rate of three groups of carbonate particles with similar intra-porosities, i.e. 0.15, 0.12 and 0.09 after pore filling, respectively. For ease of visualization, 2D cross-sectional slices of the particles prior to and after the pore filling are also presented in Fig. 12a-c. Typical pore regions that are effectively filled are marked on the CT slices. It should be noted that some pore regions are not filled by the pore
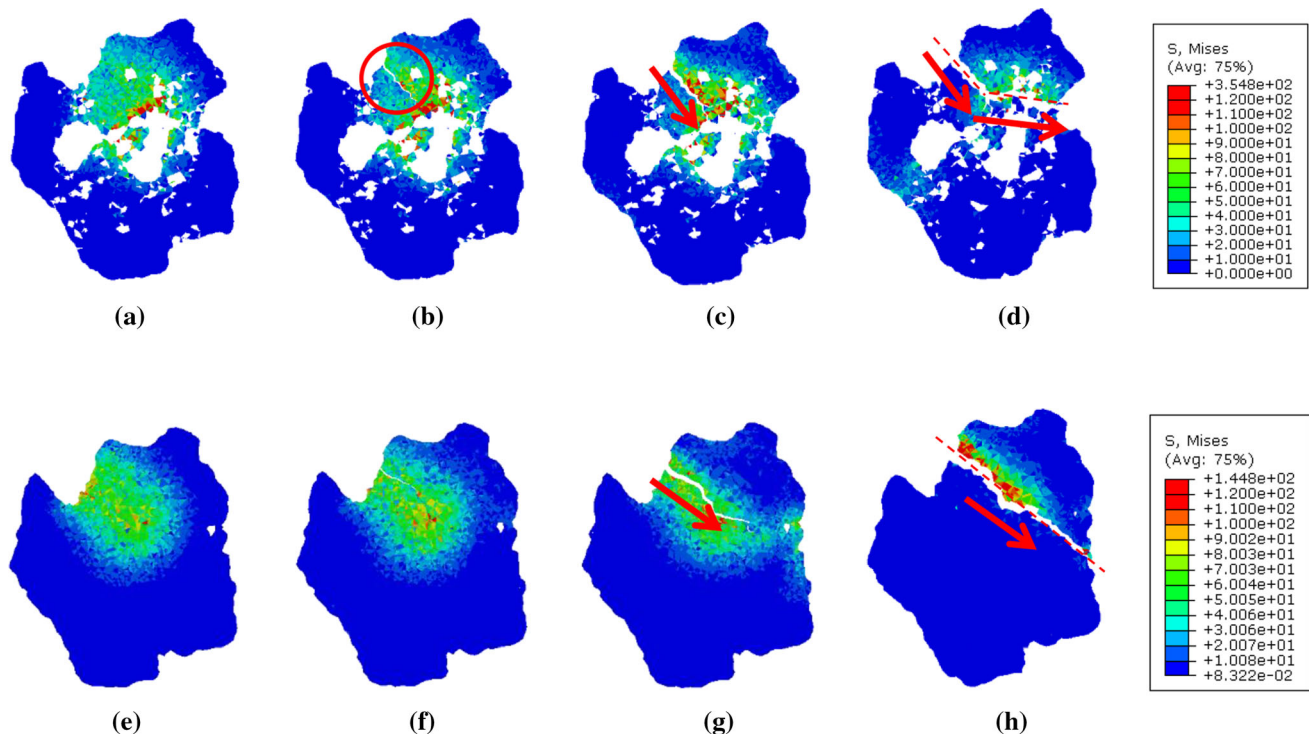
Fig. 13 Evolution of stress field (unit: MPa) and crack propagation in a 2D plane of a typical carbonate sand particle: **a–d** without pore filling; **e–h** with pore filling; the legends show the magnitudes of von Mises stresses in the plane

filling because the pores are connected to the grain external boundaries, i.e. they are open pores. It is found that for the particles with similar intra-porosities, a more localized distribution of intra-particle pores generally leads to a higher strength increase rate after pore filling.

4.2 Stress distribution and crack propagation

The combined FDEM modelling technique allows one to investigate the evolution of the stress field and crack propagation of sand particles under single-particle compression. Figure 13a–h depicts the evolution of the stress field and crack propagation in a 2D plane of a typical carbonate sand grain with and without pore filling. Before crack initiation, the particle without pore filling exhibits a significantly higher stress concentration than that with all pores filled, as shown in Fig. 13a and e. Consequently, crack initiation occurs earlier in the particle without pore filling (Fig. 13b) than in the pore-filled particle (Fig. 13f). As the loading progresses, a major crack emerges in the upper left corner of both particles and propagates towards the lower right corner of the particles (Fig. 13c and g). The particle with pore filling fails, as the major crack (dashed line) continuously propagates towards the lower right corner until passing through the entire particle, as shown in Fig. 13h. A completely different crack propagation path is observed in the particle without pore filling: the crack

(dashed line) propagates towards the right side of the particle at the late loading stage until it has completely passed through the particle (Fig. 13d). This result implies that the crack propagation direction is influenced by the intra-particle pores. This phenomenon is consistent with the fact that cracks usually propagate along the weakest path during loading [46] and the weakest path is essentially determined by the intra-particle pore structure.

4.3 Particle crushing mode

Particles can fail in various modes [11, 36, 45]. Referring to Zhao et al. [45], particle crushing can be classified into three modes: chipping, major splitting and fragmentation. Figure 14a depicts typical examples of the three particle crushing modes obtained from the FDEM simulations. Particle failure in the three modes was statistically analysed for the carbonate sands with and without pore filling, as shown in Fig. 14b. For both carbonate sands, most particles failed in the fragmentation mode. This behaviour may be associated with the highly irregular grain shape of the carbonate sands. Studies [11] have found that a higher degree of grain shape irregularity generally leads to more particles failing in the fragmentation mode. In the present study, the particles without pore filling had a higher likelihood of failing in the fragmentation mode than those with pore filling. During loading, the cracks usually passed
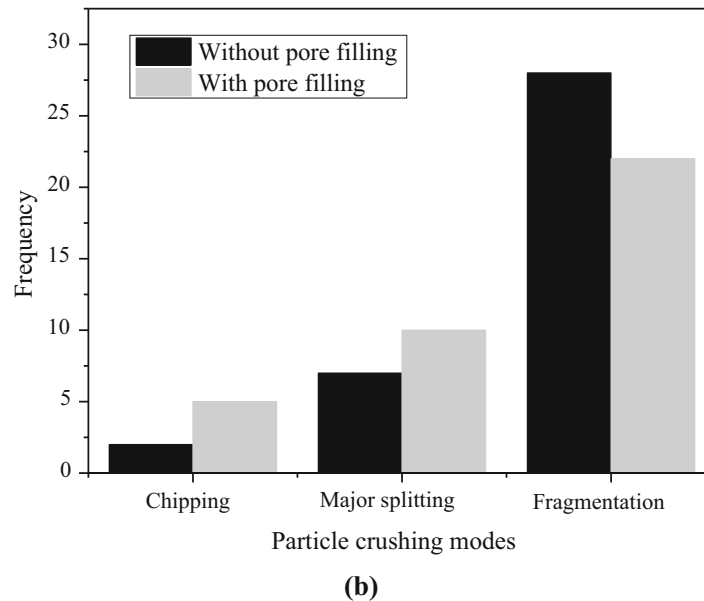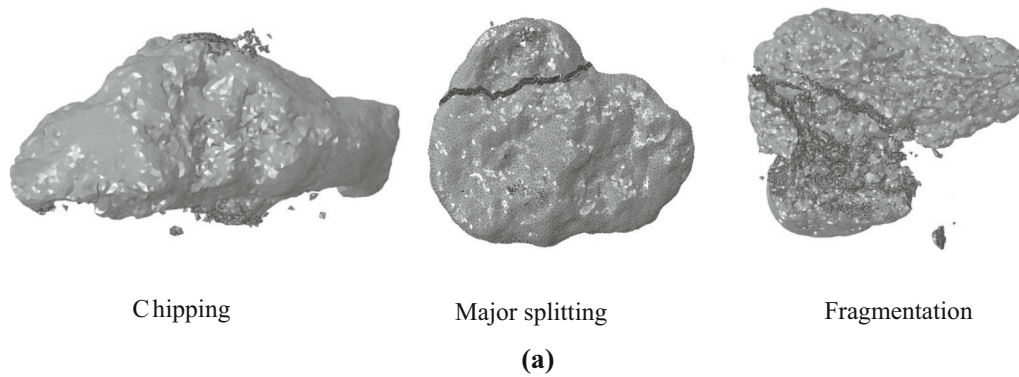
Fig. 14 Particle crushing modes: **a** typical particle crushing modes of sands in FDEM simulation; **b** frequency of different particle crushing modes

through the pore networks of the particles without pore filling, as seen in Fig. 13c and d. Consequently, more fragments were produced, and fragmentation failure occurred.

5 Conclusions

This study investigated the particle crushing behaviour of a carbonate sand under single-particle compression based on X-ray microtomography and FDEM modelling. Specifically, high-spatial-resolution X-ray μCT was applied to acquire the CT images of carbonate sand particles, from which information on the grain morphology and intra-particle pores of the sand particles was extracted and imported into the FDEM models. This allowed the modelling of carbonate sands under single-particle compression with a realistic consideration of the grain shapes and intra-particle pores. The FDEM models were calibrated by

comparing the numerical results with those observed in single-particle compression experiments of carbonate sands with in situ X-ray μCT scanning. In addition, to investigate the influences of intra-particle pores on the particle crushing behaviour, parallel FDEM simulations were implemented in which the intra-particle pores were completely filled. The following conclusions can be drawn:

(1) Combined FDEM modelling and high-spatial-resolution X-ray μCT is an effective approach to model the particle crushing behaviour of highly porous and irregularly shaped granular materials considering their realistic particle morphology and intra-particle pore geometries.
(2) The particle crushing strength is subject to a Weibull distribution for particles both with and without pore filling. The particle crushing strength can be considerably improved by filling the intra-particle pores, which is found to reduce the loading-induced stress concentration

and thereby delay the occurrence of cracks within the particles.

(3) The intra-particle pore structures have a significant influence on the crushing behaviour of porous granular materials. The intra-particle pores affect the crack propagation paths: cracks usually pass through intra-particle pores during loading, resulting in multiple fragment particles. Consequently, highly porous particles are more likely to fail in the fragmentation mode than those without intra-particle pores.

This work provides a sound basis for the modelling of the particle crushing behaviour of highly porous and irregularly shaped granular materials considering their realistic grain morphology and intra-particle pore structures. Our future research will extend this work to the modelling of the particle crushing behaviour of multiple porous granular particles under loading, for example, carbonate sands under 1D compression and triaxial compression.

References

1. API (American Petroleum Institution) (2000) Recommended practice for planning, designing, and constructing fixed offshore platforms-working stress design. Washington, DC
2. Afshar T, Disfani MM, Arulrajah A et al (2017) Impact of particle shape on breakage of recycled construction and demolition aggregates. Powder Technol 308:1–12. https://doi.org/10.1016/j.powtec.2016.11.043
3. Altuhafi FN, Coop MR (2011) Changes to particle characteristics associated with the compression of sands. Géotechnique 61:459–471. https://doi.org/10.1680/geot.9.P.114
4. Andò E, Hall SA, Viggiani G et al (2012) Grain-scale experimental investigation of localised deformation in sand: a discrete particle tracking approach. Acta Geotech 7:1–13. https://doi.org/10.1007/s11440-011-0151-6
5. Barclay DR, Buckingham MJ (2009) On the shapes of natural sand grains. J Geophys Res Solid Earth 114:1–12. https://doi.org/10.1029/2008JB005993
6. Brandes HG (2011) Simple shear behaviour of calcareous and quartz sands. Geotech Geol Eng 29:113–126
7. Cavarretta I, O'Sullivan C (2012) The mechanics of rigid irregular particles subject to uniaxial compression. Géotechnique 62:681–692. https://doi.org/10.1680/geot.10.P.102
8. Chen Y, Ma G, Zhou W et al (2021) An enhanced tool for probing the microscopic behavior of granular materials based on X-ray micro-CT and FDEM. Comput Geotech 132:103974
9. Cheng Z, Wang J (2018) Experimental investigation of inter-particle contact evolution of sheared granular materials using X-ray micro-tomography. Soils Found 58:1492–1510. https://doi.org/10.1016/j.sandf.2018.08.008
10. Cheng Z, Wang J (2018) A particle-tracking method for experimental investigation of kinematics of sand particles under triaxial compression. Powder Technol 328:436–451. https://doi.org/10.1016/j.powtec.2017.12.071
11. Cheng Z, Wang J (2021) An investigation of the breakage behaviour of a pre-crushed carbonate sand under shear using X-ray micro-tomography. Eng Geol 293:106286. https://doi.org/10.1016/j.enggeo.2021.106286
12. Cheng Z, Wang J, Coop MR, Ye G (2020) A miniature triaxial apparatus for investigating the micromechanics of granular soils with in situ X-ray micro-tomography scanning. Front Struct Civ Eng 14:357–373. https://doi.org/10.1007/s11709-019-0599-2
13. Ciantia MO, Arroyo M, Butlanska J, Gens A (2016) DEM modelling of cone penetration tests in a double-porosity crushable granular material. Comput Geotech 73:109–127. https://doi.org/10.1016/j.compgeo.2015.12.001
14. Coop MR (1990) The mechanics of uncemented carbonate sands. Géotechnique 40:607–626
15. Coop MR, Sorensen KK, Freitas TB, Georgoutsos G (2004) Particle breakage during shearing of a carbonate sand. Géotechnique 54:157–163. https://doi.org/10.1680/geot.2004.54.3.157
16. Dassault Systèmes Simulia Corp (2014) Abaqus 6.14–1: Analysis user's Manual. Providence, USA
17. Druckrey AM, Alshibli KA, Al-Raoush RI (2016) 3D characterization of sand particle-to-particle contact and morphology. Comput Geotech 74:26–35. https://doi.org/10.1016/j.compgeo.2015.12.014
18. Fang Q, Boas DA (2009) Tetrahedral mesh generation from volumetric binary and grayscale images. In: Proceedings - 2009 IEEE international symposium on biomedical imaging: From Nano to Macro, ISBI 2009. pp 1142–1145
19. Fu R, Hu X, Zhou B (2017) Discrete element modeling of crushable sands considering realistic particle shape effect. Comput Geotech 91:179–191. https://doi.org/10.1016/j.compgeo.2017.07.016
20. Hanaor D, Gan Y, Revay M et al (2016) 3D printable geomaterials. Géotechnique 66:323–332
21. Hillerborg A, Modéer M, Petersson PE (1976) Analysis of crack formation and crack growth in concrete by means of fracture mechanics and finite elements. Cem Concr Res 6:773–781. https://doi.org/10.1016/0008-8846(76)90007-7
22. Jardine R, Chow F, Overy R, Standing J (2005) ICP design methods for driven piles in sands and clays. Thomas Telford, London
23. Kawamoto R, Andò E, Viggiani G, Andrade JE (2016) Level set discrete element method for three-dimensional computations with triaxial case study. J Mech Phys Solids 91:1–13. https://doi.org/10.1016/j.jmps.2016.02.021
24. Kong D, Fonseca J (2019) On the kinematics of shelly carbonate sand using X-ray micro tomography. Eng Geol 261:1–9
25. Lv Y, Li X, Fan C, Su Y (2021) Effects of internal pores on the mechanical properties of marine calcareous sand particles. Acta Geotech 16:3209–3228. https://doi.org/10.1007/s11440-021-01223-8
26. Lv Y, Li X, Wang Y (2020) Particle breakage of calcareous sand at high strain rates. Powder Technol 366:776–787. https://doi.org/10.1016/j.powtec.2020.02.062
27. Munjiza AA (2004) The combined finite-discrete element method. John Wiley & Sons
28. Nadimi S, Fonseca J (2018) A micro finite-element model for soil behaviour: numerical validation. Géotechnique 68:364–369. https://doi.org/10.1680/jgeot.16.P.163
29. Nakata Y, Hyde AFL, Hyodo M, Murata H (1999) A probabilistic approach to sand particle crushing in the triaxial test. Géotechnique 49:567–583. https://doi.org/10.1680/geot.1999.49.5.567
30. Ostu N (1979) A threshold selection method from gray-level histograms. IEEE Trans Syst Man Cybern 9:62–66
31. Peng Y, Liu H, Li C et al (2021) The detailed particle breakage around the pile in coral sand. Acta Geotech 16:1971–1981. https://doi.org/10.1007/s11440-020-01089-2

32. Santamarina JC, Cho GC (2004) Soil behaviour: The role of particle shape. In: Advances in geotechnical engineering: The skempton conference In: Proceedings of a three day conference on advances in geotechnical engineering, organised by the institution of civil engineers. pp 604–617

33. Shi Y, Yan WM (2015) Segmentation of irregular porous particles of various sizes from X-ray microfocus computer tomography images using a novel adaptive watershed approach. Geotech Lett 5:299–305

34. Su D, Yan WM (2020) Prediction of 3D size and shape descriptors of irregular granular particles from projected 2D images. Acta Geotech 15:1533–1555. https://doi.org/10.1007/s11440-019-00845-3

35. Sukumaran B, Ashmawy AK (2001) Quantitative characterisation of the geometry of discrete particles. Géotechnique 51:619–627. https://doi.org/10.1680/geot.51.7.619.51393

36. Wang W, Coop MR (2016) An investigation of breakage behaviour of single sand particles using a high-speed microscope camera. Géotechnique 66:984–998. https://doi.org/10.1680/jgeot.15.P.247

37. Wiebicke M, Andò E, Viggiani G, Herle I (2020) Measuring the evolution of contact fabric in shear bands with X-ray tomography. Acta Geotech 15:79–93. https://doi.org/10.1007/s11440-019-00869-9

38. Wu M, Wang J, Russell A, Cheng Z (2021) DEM modelling of mini-triaxial test based on one-to-one mapping of sand particles. Géotechnique 71(8):714–727. https://doi.org/10.1680/jgeot.19.p.212

39. Wu M, Wang J, Zhao B (2021) DEM modelling of the one-dimensional compression of sands incorporating a statistical particle fragmentation scheme. Can Geotech J. https://doi.org/10.1139/cgj-2020-0557

40. Wählby C, Sintorn I-M, Erlandsson F et al (2004) Combining intensity, edge and shape information for 2D and 3D segmentation of cell nuclei in tissue sections. J Microsc 215:67–76

41. Xiao Y, Yuan Z, Chu J et al (2019) Particle breakage and energy dissipation of carbonate sands under quasi-static and dynamic compression. Acta Geotech 14:1741–1755. https://doi.org/10.1007/s11440-019-00790-1

42. Xiong W, Wang J, Cheng Z (2020) A novel multi-scale particle morphology descriptor with the application of SPHERICAL harmonics. Materials 13(15):3286. https://doi.org/10.3390/MA13153286

43. Xu WJ, Liu GY, Yang H (2020) Study on the mechanical behavior of sands using 3D discrete element method with realistic particle models. Acta Geotech 15:2813–2828. https://doi.org/10.1007/s11440-020-00982-0

44. Xu XP, Needleman A (1995) Numerical simulations of dynamic crack growth along an interface. Int J Fract 74:289–324. https://doi.org/10.1007/BF00035845

45. Zhao B, Wang J, Andò E et al (2020) An investigation of particle breakage under one-dimensional compression of sand using X-ray micro-tomography. Can Geotech J 57:754–762

46. Zhao B, Wang J, Coop MR et al (2015) An investigation of single sand particle fracture using X-ray micro-tomography. Géotechnique 65:625–641. https://doi.org/10.1680/geot.4.P.157

47. Zheng J, He H, Alimohammadi H (2021) Three-dimensional Wadell roundness for particle angularity characterization of granular soils. Acta Geotech 16:133–149. https://doi.org/10.1007/s11440-020-01004-9

48. Zheng J, Hryciw RD (2015) Traditional soil particle sphericity, roundness and surface roughness by computational geometry. Géotechnique 65:494–506. https://doi.org/10.1680/geot.14.P.192

49. Zhou B, Ku Q, Wang H, Wang J (2020) Particle classification and intra-particle pore structure of carbonate sands. Eng Geol 279:105889. https://doi.org/10.1016/j.enggeo.2020.105889

50. Zhou B, Wang J, Wang H (2018) Three-dimensional sphericity, roundness and fractal dimension of sand particles. Géotechnique 68:18–30. https://doi.org/10.1680/jgeot.16.P.207

51. Zhou B, Wang J, Wang H (2018) A novel particle tracking method for granular sands based on spherical harmonic rotational invariants. Géotechnique 68:1116–1123. https://doi.org/10.1680/jgeot.17.t.040

52. Zhou B, Wang J, Zhao B (2015) Micromorphology characterization and reconstruction of sand particles using micro X-ray tomography and spherical harmonics. Eng Geol 184:126–137. https://doi.org/10.1016/j.enggeo.2014.11.009

53. Zhou B, Wei D, Ku Q et al (2020) Study on the effect of particle morphology on single particle breakage using a combined finite-discrete element method. Comput Geotech 122:103532. https://doi.org/10.1016/j.compgeo.2020.103532